# Cross-flow structured packing for the process intensification of post-combustion carbon dioxide capture

Chemical Engineering Science 178 (2018) 284–296

Contents lists available at ScienceDirect

Chemical Engineering Science

journal homepage: www.elsevier.com/locate/ces

# Cross-flow structured packing for the process intensification of post-combustion carbon dioxide capture

Gianluca Lavalle [a,1], Mathieu Lucquiaud [a], Marc Wehrli [b], Prashant Valluri [a,*]

[a] School of Engineering, University of Edinburgh, Edinburgh EH9 3JG, United Kingdom
[b] Sulzer Chemtech Ltd, 8404 Winterthur, Switzerland

## HIGHLIGHTS

- A cross-flow cell of structured packing is inspected for carbon capture.
- Pressure drop and flow repartition are investigated numerically.
- The onset of flooding is shown to be delayed by tilting the cell.

## ARTICLE INFO

*Article history:*
Received 17 May 2017
Received in revised form 1 November 2017
Accepted 13 December 2017
Available online 22 December 2017

*Keywords:*
Gas-liquid flow
Cross-flow
Flooding
CFD
Structured packings
Carbon capture

## ABSTRACT

We introduce novel insights into a cross-flow arrangement of structured packings specifically for post-combustion carbon dioxide capture. Gas-liquid dynamics are investigated numerically, with the liquid flowing under the action of the gravity and the gas driven by a horizontal pressure gradient crossing the liquid phase. An elementary packing cell consists of two connected channels: one depicting a co-current gas-liquid flow and the other depicting a counter-current two-phase flow. While flow reversal of the liquid phase can occur in the counter-flow channel at high gas flow rates, the overall flooding point is significantly delayed in comparison to a counter-current flow arrangement traditionally used for structured packings. Varying the gas flow rate and the tilting angle of the elementary cell, a detailed numerical analysis of the flow repartition between channels, the pressure drop, the gas and liquid velocities, and the onset of flooding is presented. The pressure drop is found to be smaller when tilting the cell with respect to the initial scenario at 45°. Flow reversal instead is delayed when lowering the tilting angle, that is when the cell is tilted anti-clockwise. We also reveal the presence of long waves at the edge of the cell at low tilting angles. Finally, data of the wet pressure drop in the cross-flow cell are compared with different commercially available types of packing arranged in a conventional vertical counter-flow configuration, such as several versions of the Sulzer Mellapak™.


## 1. Introduction

Gas-liquid flows play a fundamental role in many chemical unit operations, such as the carbon dioxide absorption and distillation columns. To enhance gas-liquid contact, common column internals used are structured packings. These optimised geometric structures, made of textured metal sheets to maximise interfacial contact area between a gas phase and a liquid phase, spread the liquid phase as a thin film to extend residence time and allow mass transfer and chemical reactions to complete. The resulting flow occurring in the alignment of these packings is a counter-current flow. Here, a gravity-driven falling liquid film flows downwards along the packing walls in the presence of an upward flowing gas at a constant pressure gradient (driven from the bottom of the column). A typical application being removal of $CO_2$ from flue-gas using an amine solution in an absorption column.

Any such gas-liquid configuration is inherently unstable and the primary instability is manifested as interfacial waves (Craik, 1966; Yih, 1967). The primary source of the instability is the so-called interfacial mode driven by viscosity contrast between the phases (Boomkamp and Miesen, 1996). Here, the instability kicks off as an infinitesimally small wave, growing exponentially (by virtue of a linear instability) in amplitude both in time and space

* Corresponding author.
*E-mail addresses:* gianluca.lavalle@limsi.fr (G. Lavalle), m.lucquiaud@ed.ac.uk (M. Lucquiaud), Marc.Wehrli@sulzer.com (M. Wehrli), prashant.valluri@ed.ac.uk (P. Valluri).
[1] Present address: LIMSI, CNRS, Université Paris-Saclay, Bât. 508, Campus Universitaire, F-91405 Orsay, France.

https://doi.org/10.1016/j.ces.2017.12.022
0009-2509/

(Lavalle et al., 2017; Schmidt et al., 2016; Tilley et al., 1994; Valluri et al., 2010; Vellingiri et al., 2015). At large amplitudes, growth tends to be non-linear, with energies derived from the inertia of both the phases (the shear modes) in addition to the interfacial mode. This causes the waves to be distorted, leading to formation of ligaments that tend to break-off into droplets carried by the upward gas current. Interfacial waves of this kind play an important role towards enhancing available exchange area, which is crucial for mass and heat transfer (Henstock and Hanratty, 1979; McCready and Hanratty, 1985). However, any counter-current gas-liquid flow is limited by its practical operability. Specifically, at high gas loads, flow reversal occurs in the liquid phase, resulting in the column being flooded by the liquid. This event is called flooding and is characterised by high pressure drops. Therefore, it is common practice in the industry to run the absorption column below the flooding onset point, in order to get the best fruition of the mass transfer at smaller pressure drops. Nevertheless, at the same transfer efficiency, one would delay the flooding onset in order to reduce size and cost of these equipments.

The flow in structured packing has been the subject of many experimental and numerical studies in the past. The experimental works have focussed either on the analysis of performances of novel structured packings (Olujić et al., 2003; Bessou et al., 2010), or the influence of the liquid physical properties on the wetted area (Nicolaiewsky et al., 1999; Bradtmöller et al., 2015); further experimental works have been also performed to measure the liquid spreading in structured packings (Aferka et al., 2011; Fourati et al., 2012). Recently, Computational Fluid Dynamics (CFD) has become an effective tool to complement the experimental works, although the computational cost might still be too expensive for the analysis of complex geometries such as the entire column. Raynal and Royon-Lebeaud (2007) have developed an approach where two-dimensional gas-liquid CFD results are used as basis for three-dimensional one-phase simulations involving the whole column geometry. Subsequently, Fernandes et al. (2009) have performed CFD simulations of a pseudo single-phase model aiming to study the wet pressure drop inside the Sulzer EX structured gauze packing. Several studies have also focussed on the inspection of flow pattern, liquid hold-up and mass transfer occurring in film flows over a packing substrate (Haroun et al., 2010; Valluri et al., 2005; Xu et al., 2008); other works have aimed to characterize the three-dimensional liquid flow over a structured packing element (Ataki and Bart, 2006).

Simultaneously, many studies have investigated the flooding onset in structured packing. Beginning with the empirical method proposed by Sherwood et al. (1938), new analytical approaches have followed (Dankworth and Sundaresan, 1989; Hutton et al., 1974; Iliuta et al., 2014). Meanwhile, flooding has been extensively examined in two-dimensional liquid films sheared by laminar or turbulent gas flows by means of linear stability, Direct Numerical Simulation (DNS) and reduced-order film models (Trifonov, 2010; Tseluiko and Kalliadasis, 2011; Dietze and Ruyer-Quil, 2013; Schmidt et al., 2016; Lavalle et al., 2017; Vellingiri et al., 2015). However, these methods cannot be directly transferred to structured packings due to the flat wall geometries considered in those studies (Hutton et al., 1974).

In this article, we investigate the gas-liquid flow in a cross-flow arrangement of structured packing for post-combustion carbon capture. Post-combustion carbon capture requires removing carbon dioxide from large volumetric flow rates of combustion gas streams at close to atmospheric pressure. One way to achieve process intensification (defined here as a series of design strategies implemented to achieve drastic reductions in the size of existing processes) is to increase gas flow rates to reduce the resulting cross-sectional area and height of $CO_2$ absorption packed columns. In practice, the cross-sectional area could match a typical heat recovery steam generator structure of a Combined Cycle Gas Turbine or the horizontal ducting downstream of pulverised coal boiler. In this work, we show that horizontal, cross-flow packed column configurations are likely to delay, at increasing gas flow rates, the occurrence of flow reversal in the liquid phase (characterised by high pressure drops) and can be operated at higher gas velocities than conventional, vertical counter-flow configurations. Horizontal absorbers are currently used in smaller scale application in gas-air treating, and at scale for Flue Gas Desulphurisation (FGD) of combustion gases (Klingspor et al., 2002), although with liquid spray systems instead of packing material. The application to carbon capture is novel and is the focus of this article.

While in a conventional vertical packed column the gas is injected from the bottom and ejected at the top, in the cross-flow packing the gas instead flows from left to right under a horizontal pressure gradient. In both scenarios the liquid falls as a thin film driven by the gravity. While vertical counter-flow arrangements are more common, certain applications such as post-combustion $CO_2$ capture could present favourable characteristics for cross-flow horizontal packed columns: (i) less visual impact at the power plant level because the absorber could develop horizontally rather than vertically; (ii) the absorber could be directly integrated in the flue gas pathway with rectangular ducting.

In order to provide novel insights into the cross-flow arrangement, we present the first detailed CFD study of the gas-liquid flow within a three-dimensional elementary cell of such an alignment of structured packings, as shown in Fig. 1, where the gas flows parallel to the packing sheets. The choice of modeling one single elementary cell aims to reduce the computational cost; this issue has been already discussed by Petre et al. (2003) and Raynal et al. (2004) when simulating the dry pressure drop in structured packings. Also, Said et al. (2011) have shown that modeling the dry pressure drop within a periodic elementary cell is a good representation for the whole packing.

Our two-phase model is based on the Volume-of-Fluid (VoF) method with a Smagorinsky LES (Large Eddy Simulation) model for the turbulent terms. Validation of this transient two-phase VoF-LES model is achieved by comparing the pressure drop of the classical vertical cell under counter-current flow with previous experimental works, and with industrial data from the Sulcol 3.2

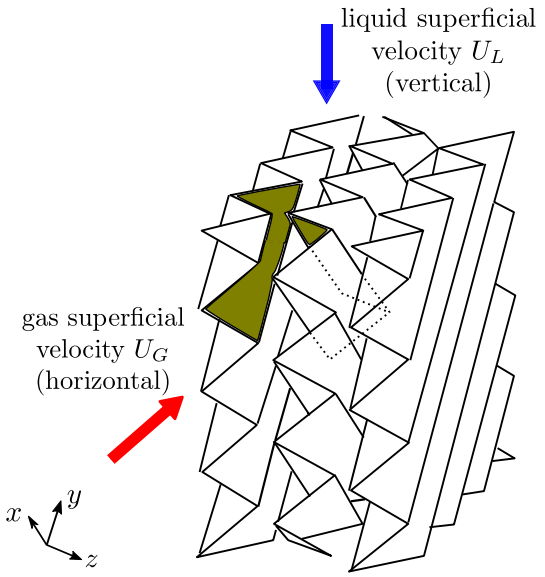


**Fig. 1.** Representation of the cross-flow structured packing. The highlighted and dashed area corresponds to the elementary cell considered here, and depicted in Fig. 2.

software by Sulzer Chemtech. Aiming to carry out a first step towards optimisation of such a cross-flow elementary cell, we examine the fundamental behaviour of the flow to estimate key performance metrics, such as pressure drop, interfacial area, film thickness, liquid and gas distribution. Particularly, the analysis of the averaged liquid velocity in the counter-flow channel gives indication of the flooding onset. We reveal that tilting the cell in an anti-clockwise fashion reduces the pressure drop and delays the flooding onset. We also show that the gas is found to preferentially escape upwards rather than flowing horizontally. These metrics will inform the optimisation, design and scale-up of cross-flow $CO_2$ absorber systems, as part of a wider programme of research at the University of Edinburgh. Finally, the computed net pressure drops are compared against industrial packings available in the literature.

The paper is organised as follows: Section 2 presents the framework under investigation; Section 3 describes the numerical formulation and its validation, whereas Section 4 the main results; finally, Section 5 shows comparisons with industrial packings, before conclusions (Section 6).

## 2. The general framework

We consider a three-dimensional cross-flow elementary cell of a structured packing, as depicted in the shaded area of Fig. 1. A structured packing consists of a series of textured metal sheets connected together and with opposite orientation of their triangular channels. In the present case, the channels cross at a constant angle of 90°. The elementary cell is a periodic geometric pattern which repeats itself: this is sketched in Fig. 2. Like the conventional vertical packing, the liquid flows from the top to the bottom under the action of the gravity. The gas instead flows from left to right driven by an applied pressure gradient, rather than from bottom to top as in conventional vertical packings. Fig. 2 also shows that gas and liquid flow in a co-current fashion in one of the two connected channels of the cell, and in a counter-current way in the other. This is an important and distinguishing feature of the cross-flow cell, whereas in the usual vertical cell both channels are counter-current. Since flooding occurs under certain conditions in counter-current gas-liquid flows, the presence of the co-current channel might delay the flooding onset and widen the operation of the cross-flow cell in applications such as post-combustion carbon capture, to be shown is Section 4.2.

The sheets of structured packings have textured walls and perforations all along. The former help to destabilize the liquid film and increase the exchange area between the two phases, aiming to enhance the mass transfer. The latter instead allow the liquid to drain across the packing and prevent from its accumulation. In this study, we have not represented the textures and the perforations within the elementary cell, and leave this subject to future studies.

The chosen fluids are typical of the $CO_2$ absorption process and the corresponding properties are listed in Table 1. The liquid is an aqueous solution of monoethanolamine (MEA) at 30% in weight at 25 °C, see Amundsen et al. (2009) and Jayarathna et al. (2013). The gas phase is instead the flue gas at ambient temperature. From Fig. 2, the definitions to be used throughout this study are:

- equivalent diameter of the cell $D = 4A/p_w = 5.25$ mm, where $A = 4.03 \cdot 10^{-5}$ m$^2$ is the area of the inlet (triangle with base $\delta = 0.0127$ m) and $p_w = 3.07 \cdot 10^{-2}$ m the wetted perimeter (perimeter of the triangle). The equivalent diameter of the elementary cell is a very close approximation of real packing dimensions, such as the Sulzer Mellapak™ 500.Y (whose equivalent diameter is $D = 5$ mm). The reason for this discrepancy is because the presence of the geometrical structure on the packing surface is not considered. This surface structure could be represented by a sinusoidal surface of an amplitude typically 5–10% of the equivalent diameter of the unit cell;
- inclination of the cell $\beta$ around the $x$ axis, to be varied (for the base configuration we have $\beta = 45°$). Note that the angle between crossing channels always remains at 90°;
- characteristic length $L = \delta \cos\beta$ used for the definition of the dry and wet pressure drops, to be defined later;
- Reynolds number of the gas phase $Re_G = U_G D/\nu_G$ imposed on the left, where $U_G$ is the horizontal and superficial gas velocity, whereas $\nu_G$ the gas kinematic viscosity;
- superficial liquid velocity $U_L$ imposed at the top.

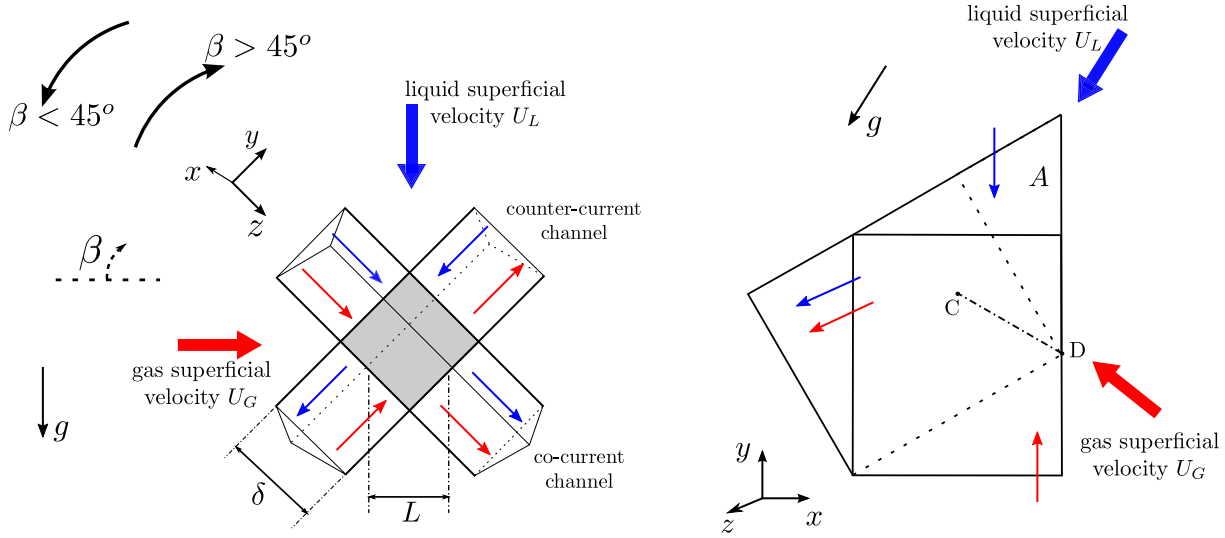


**Fig. 2.** Schematic diagram of the cross-flow elementary cell, with the counter-flow channel along the $y$-direction and the co-flow channel along the $z$-direction. The former is in the back whereas the latter in the front. The liquid is indicated in blue whereas the gas in red (block arrows define the superficial velocity while simple arrows the velocity within the channels); the angle $\beta$ is the tilting angle. The grey-shaded area defines the computational domain, which is zoomed in on the right hand side. The point $C$ is the centre of the cell, whereas the segment $\overline{CD}$ in the counter-flow channel is the line where the velocity profiles are plotted in Figs. 11 and 12. (For interpretation of the references to colour in this figure legend, the reader is referred to the web version of this article.)

**Table 1**
Physical properties of the liquid and the gas phases.

| fluid | $\rho$ (kg m$^{-3}$) | $\mu$ ($10^{-4}$ Pa s) | $\gamma$($10^{-3}$ N m$^{-1}$) | $\rho_2/\rho_1$ | $\mu_2/\mu_1$ |
|---|---|---|---|---|---|
| MEA-water (30%) | 1080 | 20 | 62.2 | $1.06 \cdot 10^{-3}$ | $8.5 \cdot 10^{-3}$ |
| Flue gas | 1.145 | 0.17 | | | |

As a general convention in absorption an distillation, the gas load is reported using the F-factor $F = U_G\sqrt{\rho_G}$, where $\rho_G$ is the gas density; following Grünig et al. (2013), the liquid load is defined as $B = U_L A/S$, where $S = 4.58 \cdot 10^{-4}$ m$^2$ is the surface area of the wall of the computational domain. In absorption and distillation applications, the F-factor lies in the range $F = 0.1 - 6\sqrt{\text{Pa}}$, whereas the liquid load $B = 0.2$—$200$ m$^3$/(m$^2$ h), see for example structured packings by Sulzer Chemtech, such as Mellapak™ 250. Y and Mellapak 500.Y (Spiegel and Meier, 1992). In this work we use values of gas and liquid velocities such that we test the cross-flow absorber in the range of real applications. The aim of this study is to characterize the flow in such a cross-flow absorber cell and analyse the performance in terms of pressure drop, flow repartition and flooding onset.

We have tested three different gas velocities (see Table 2), five tilting angles for each gas velocity to balance flow repartition between the two channels of the cell, and two liquid loads to inspect the influence on the flooding onset.

## 3. Description and validation of the numerical model

### 3.1. The numerical model

Owing to the complex geometry being considered, we develop a transient (unsteady) VoF-LES model using Ansys CFX™. The VoF approach applies an Eulerian description of each phase on a fixed grid, and the interface between the two phases is computed through the transport equation of the local volume fraction (Scardovelli and Zaleski, 1999). The two phases are assumed to be Newtonian, incompressible and isothermal, the phase change being neglected. Reactions at the gas-liquid interface are also neglected. The two-phase unsteady flow is governed by the Navier-Stokes equations

$$\nabla \cdot \mathbf{u} = 0, \tag{1a}$$
$$\rho(\partial_t \mathbf{u} + \mathbf{u} \cdot \nabla \mathbf{u}) = -\nabla p + \rho \mathbf{g} + \nabla \cdot \mathbf{T} - \gamma \kappa \mathbf{n} \delta_i, \tag{1b}$$

where $\mathbf{u}$ is the velocity vector, $\rho$ and $p$ the local density and pressure, respectively, $\mathbf{g} = (0, -g\cos\beta, g\sin\beta)^T$ the gravity vector, and $\mathbf{T} = \mu(\nabla \mathbf{u} + \nabla \mathbf{u}^T)$ the viscous stress tensor. The surface tension is defined with $\gamma$, whereas the curvature with $\kappa = \nabla \cdot \mathbf{n}$, where $\mathbf{n} = \nabla\varphi/|\nabla\varphi|$ represents the unit normal vector; $\delta_i$ is instead the Dirac delta function. The volume fraction $\varphi$, which provides information of the location of both phases ($\varphi = 0$ in the gas and $\varphi = 1$ in the liquid), is advected via the equation

$$\partial_t \varphi + \mathbf{u} \cdot \nabla \varphi = 0. \tag{2}$$

Local density and viscosity can be computed with

$$\rho = \varphi\rho_L + (1-\varphi)\rho_G, \tag{3a}$$
$$\mu = \varphi\mu_L + (1-\varphi)\mu_G, \tag{3b}$$

**Table 2**
Gas-phase Reynolds numbers with corresponding horizontal gas velocities and F-factor used in this study for the dry simulations.

| | Test 1 | Test 2 | Test 3 |
|---|---|---|---|
| $Re_G$ | 682 | 1259 | 1937 |
| $U_G$ (m/s) | 1.93 | 3.55 | 5.47 |
| $F$ ($\sqrt{\text{Pa}}$) | 2.06 | 3.80 | 5.85 |

where subscripts $L$ and $G$ refers to liquid and gas, respectively. The Continuum Surface Force (CSF) method is applied to model the surface tension (Brackbill et al., 1992). A Large Eddy Simulation (LES) method is used to model the turbulence in the gas, with the Smagorinsky model for the near-wall analysis (Smagorinsky, 1963). Velocity and pressure fields are filtered at the sub-grid scale and all the small-scale structures below this filter are modelled.

Filtering Eqs. (1) leads to

$$\nabla \cdot \bar{\mathbf{u}} = 0, \tag{4a}$$
$$\bar{\rho}(\partial_t \bar{\mathbf{u}} + \bar{\mathbf{u}} \cdot \nabla \bar{\mathbf{u}}) = -\nabla \bar{p} + \bar{\rho}\mathbf{g} + \nabla \cdot (\bar{\mathbf{T}} + \boldsymbol{\tau}) - \gamma \bar{\kappa} \bar{\mathbf{n}} \delta_i + \mathscr{E}, \tag{4b}$$
$$\partial_t \bar{\varphi} + \bar{\mathbf{u}} \cdot \nabla \bar{\varphi} = 0, \tag{4c}$$

where the bar defines the filtered fields. Two additional terms appear in the momentum equation upon the filtering process. The first represents the residual stress tensor and is defined as $\bar{\tau}_{ij} = \overline{u_i u_j} - \bar{u}_i \bar{u}_j$. The second term $\mathscr{E}$ accounts for the sum of all the errors resulting from the subgrid-scale terms, including also the filtered surface tension, and can be neglected (Liovic and Lakehal, 2007a; Labourasse et al., 2007). The Smagorinsky model is used to close the resulting filtered equation, allowing to express the residual stress tensor as

$$\tau_{ij} = 2\mu_t s_{ij}, \qquad s_{ij} = \frac{1}{2}(\partial_{x_j}\bar{u}_i + \partial_{x_i}\bar{u}_j), \tag{5}$$

where $\mu_t$ is the eddy viscosity, given by

$$\mu_t = (C_s\Delta)^2|\bar{s}|, \qquad |\bar{s}| = \sqrt{2\bar{s}_{ij}\bar{s}_{ij}}, \tag{6}$$

where $C_s = 0.18$ is the Smagorinsky constant, whereas $\Delta$ is the length of the unresolved scale, which is generally chosen as the grid size, i.e. $\Delta = 2(\Delta x \Delta y \Delta z)^{1/3}$ (Abbott and Basco, 1989). Once the Smagorinsky model is added to the filtered momentum Eq. (4b), it leads to

$$\bar{\rho}(\partial_t \bar{\mathbf{u}} + \bar{\mathbf{u}} \cdot \nabla \bar{\mathbf{u}}) = -\nabla \bar{p} + \bar{\rho}\mathbf{g} + \nabla \cdot (\bar{\mathbf{T}} + \boldsymbol{\tau}) - \gamma \bar{\kappa} \bar{\mathbf{n}} \delta_i, \tag{7}$$

where now $\boldsymbol{\tau}$ is given by Eqs. (5) and (6). Finally, the velocity vector vanishes for both phases at the wall. Here, we adopt a wall adhesion model with imposed contact angle of 0° so that the fluid is fully wetting. The VoF method used ensures that there is continuity of velocity and tangential stress at the gas-liquid interface.

A mesh-independence test over Nusselt film thickness has indicated an optimum computational domain with 2-million elements and with biased refinement close to the walls such that the liquid film is adequately resolved (Fig. 3).

Here we discuss the Smagorinsky model chosen for resolving turbulence. As a general rule, we ensure that the cell size in the liquid never exceeds $h_0/10$, where $h_0$ is the Nusselt film thickness defined later in Eq. (8). To this end, we have also tested a maximum cell size in the liquid phase smaller than $h_0/20$ and found no remarkable differences of the flow pattern in the vicinity of the interface. However, in presence of interfacial waves the scenario changes: while the trough of the wave approaches the wall, the wave crest might leave the region of refined mesh causing a lower accuracy of the near-wall law. This effect could also occur at the edge of the cross-flow cell, where an accumulation of the liquid is expected. A film thinner than the mesh-cell could be subject to numerical break-up, hence we stop our simulations (especially the ones with low liquid load) before the film breaks. Nevertheless, it must be recalled that capturing the flow correctly at the interface

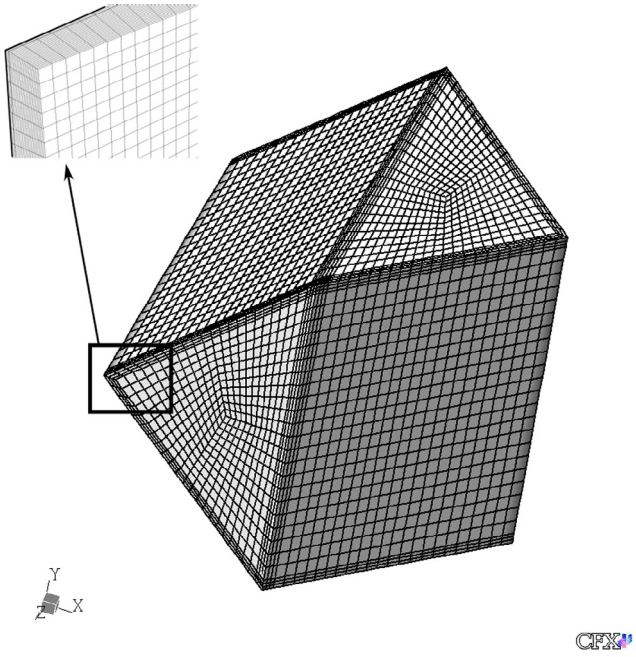


**Fig. 3.** Computational mesh and geometry of a representative structured packing (very close approximation of Mellapak 500.Y) unit cell. Inset shows refined mesh near the wall.

between a wavy liquid film and a turbulent gas flow, and the so-called interfacial LES model to quantify eddies in the near-interface region, still remains an open issue (Belcher and Hunt, 1998; Labourasse et al., 2007; Liovic and Lakehal, 2007a,b).

The discretization scheme is second-order central difference in space and second-order backward Euler in time. The time step used in the simulations is adaptive and never greater than $1 \cdot 10^{-5}$ s allowing to fulfill the condition $\Delta t = \min[t_c, t_\nu]$, where $t_c = \Delta x_{min}/U_G$ is the convective time-scale and $t_\nu = \Delta x_{min}^2/\nu_L$ corresponds to the viscous time-scale, $\Delta x_{min}$ being the finest mesh size. MPI parallelization allows us to perform the run with up to 64 cores.

We adopt a two-step numerical strategy:

1. first a "dry scenario", where we evaluate the dynamics of the gas phase. We use inlet-outlet boundary conditions, by imposing the velocity at the inlet and the ambient pressure at the outlet. This step of the simulation allows us to estimate the dry pressure drop, 3D velocity and pressure fields inside the cell. This is a crucial step as these results provide accurate initial conditions (for velocity and pressure fields) for the two-phase wet simulations in the second step;
2. in the second step, we consider an unsteady "wet scenario", where both the liquid and the gas are considered. The pressure and velocity distributions obtained from the dry simulation in the first step are given as initial conditions. In addition, it is also necessary to specify the initial position of the gas-liquid interface in the domain. This is done by imposing a flat film at $t = 0$ with the initial film thickness set by the Nusselt relation at the imposed liquid load $B$ (Nusselt, 1916):

$$h_0 = \sqrt[3]{\frac{3\nu_L B w}{g \sin\beta}}, \tag{8}$$

where $w = 1.8 \cdot 10^{-2}$ m is the width of the cell considered as a plain flat plate. Here we implement periodic boundary conditions with imposed pressure drops (as computed from the first-step strategy) at the boundaries of the domain. The pressure drops must be imposed such that the flow directions are in accordance with the cross-flow geometry as shown in Fig. 2. Periodic boundary conditions are necessary to represent the unit cell as a repetitive arrangement in a large system (such as that of an absorption column). Periodic boundary conditions are appropriate representation of flows far from the inlet and outlet of the column, and provide a considerable reduction of the computational cost.

The resulting transient two-phase VoF-LES model allows us to fully capture the two-phase flow dynamics within the cross-flow elementary cell. However, given that the periodic boundary conditions in the wet scenario accounts for an imposed pressure gradient, the resulting gas-liquid flow pattern will adapt to this imposed value, which in turn corresponds to the pressure drop obtained through the dry simulation. Thus, the solution obtained is the two-phase flow pattern (interface shape including waves, local 3D velocity vector and pressure) at a fixed pressure drop. Here we explain the procedure which allows us to obtain the wet pressure drop when using periodic boundary conditions with imposed pressure drop of the dry scenario: in reality, at fixed gas load (i.e. at fixed F-factor) the wet pressure drop is greater than the dry pressure drop; instead, at fixed pressure drop, the resulting F-factor in the wet column is lower than the dry column. In our case, the dry pressure drop is imposed as boundary condition for the wet-stage simulation and the increase of pressure drop cannot be captured. However, the wet pressure drop can be obtained *a posteriori* by quantifying the reduction, within the cell, of the F-factor in the wet configuration with respect to the dry scenario. This is accomplished by computing, at the end of the run, the averaged gas velocity at the outlet plane of each channel. This velocity is then recomposed in the horizontal direction, and gives the wet F-factor, as shown in Table 5. This velocity recomposition is consistent with the velocity decomposition that is performed at the inlet for the dry scenario. We remark also that the effect of lowering the F-factor is more pronounced at higher liquid loads.

A rigorous validation of this two-step strategy is presented in Section 3.3: it shows a thorough comparison of pressure drop for a standard counter-current flow arrangement against data available in the literature and industrial data from the Sulcol 3.2 software by Sulzer Chemtech.

### 3.2. Dry-stage simulation with cross-flow and validation

In the definition of the dry simulation for the three tests of Table 2, the gas velocity at the inlet of both channels can be computed as vector decomposition at a given tilting angle $\beta$. Numerical convergence is deemed to be achieved at a residual tolerance of $1 \cdot 10^{-6}$, after which the pressure difference $\Delta p = p_{out} - p_{in}$ in both channels is computed. This is listed in Table 3 for the counter-current and the co-current channels, respectively. One notes that the pressure drop is the same in the two channels due to the absence of the liquid phase.

Also presented in Table 3 is the dry pressure drop, measured as

$$G_{dry} = \frac{\Delta p_y + \Delta p_z}{2L}, \tag{9}$$

where $L$ is a characteristic length consisting of the distance between the channel outlets defined in Fig. 2, whereas $\Delta p_y$ and $\Delta p_z$ are the pressure drop computed in the counter-current and co-current channels, respectively. We note from Table 3 that the overall pressure drop increases with the gas velocity. Finally, we have measured the mass flow $q$ at the outlet of each channel and checked the gas repartition with respect to the total mass flow $Q_{dry}$ at the inlet. As

**Table 3**
External velocity $U_G$, pressure drop $G_{dry}$ and mass flow channel repartitions $q/Q_{dry}$ for the dry simulation (gas only). The pressure drop in the counter-current and co-current channels are defined by $\Delta p_y$ and $\Delta p_z$, respectively. The last column quantifies the deviation of the numerical mass flow $Q$ from the theoretical value $Q_{exact} = 2A\rho_G U_G$.

| $Re_G$ | $U_G$ (m/s) | $\Delta p_y$ (Pa) | $\Delta p_z$ (Pa) | $G_{dry}$ (Pa/m) | $q_y/Q_{dry}$ | $q_z/Q_{dry}$ | error (%) |
|---|---|---|---|---|---|---|---|
| 682 | 1.93 | −1.10 | −1.10 | −122.3 | 0.5 | 0.5 | 0.78 |
| 1259 | 3.55 | −3.21 | −3.21 | −357.3 | 0.5 | 0.5 | 0.78 |
| 1937 | 5.47 | −6.99 | −6.99 | −778.4 | 0.5 | 0.5 | 0.78 |

expected from the dry-stage simulation, Table 3 shows that the gas distributes evenly in each channel.

In order to validate our simulations in the dry regime, the discrepancy of the numerical mass flow at the outlet has been quantified against the exact value imposed at the inlet, i.e. $Q_{exact} = 2A\rho_G U_G$, where $A$ is the inlet area, as depicted in Fig. 2. Table 3 shows that the error, computed as $|Q - Q_{exact}|/Q_{exact}$, is smaller than 1% for all the performed numerical tests.

### 3.3. Wet-stage validation with counter-current flow

Neither experimental nor numerical work is currently available for the validation of simulations in the wet regime of cross-flow packing. Therefore, we validate the transient two-phase VoF-LES model against results in a conventional vertical counter-current packing reported in the literature. The computational domain and the mesh are the same as those depicted in Figs. 2 and 3, with the exception that the gas is injected at the bottom rather than from the left. The imposed liquid load is $B = 50\ \mathrm{m^3/(m^2\ h)}$, whereas the F-factor ranges from 0 to 10. The resulting overall pressure drop is compared against the industrial data of a Mellapak 500.Y column obtained with the software Sulcol 3.2 developed by Sulzer Chemtech. This comparison is depicted in Fig. 4, where one notices that our transient two-phase VoF-LES model applied to an elementary cell returns a similar trend with respect to the data obtained for the whole column, although shows a significative deviation for high F-factors. In particular, at low F-factors, i.e. up to $F = 0.4\sqrt{\mathrm{Pa}}$, the simulated wet pressure drop differs of almost 18% from the experimental data of the whole column. At high F-factors instead, the deviation in the wet pressure drop is greater; nevertheless, we note that the linear fit between numerical and experimental data has a similar slope, with maximum deviation of 39% in the F-factor (at the same pressure drop). However, it must be recalled that this VoF-LES model neglects the textures and the perforations at the wall of the packing. In addition, the

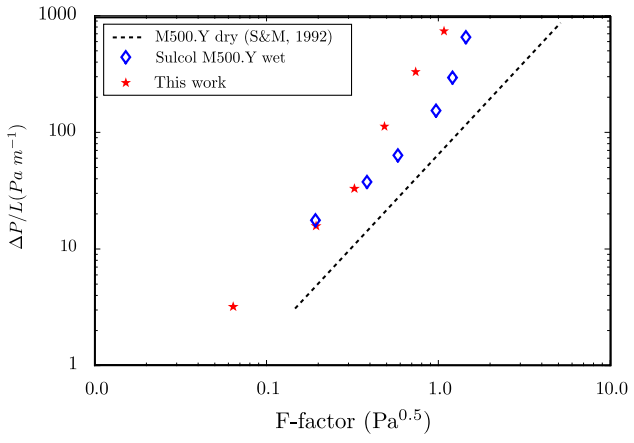


**Fig. 4.** Comparison of the pressure drop at a liquid load of 50 $\mathrm{m^3/m^2/h}$ between our transient two-phase VoF-LES model for Mellapak 500.Y in the conventional vertical counter-flow configuration, and data from the software Sulcol 3.2 by Sulzer. The dashed line refers to the dry pressure drop of Mellapak 500.Y from Spiegel and Meier (1992) (S&M, 1992 in the legend).

observed deviation in the wet pressure drop might be due to the choice of the periodic elementary cell, in view of the fact that Haroun and Raynal (2016) have showed a 20% deviation for a wide range of F-factors of the simulated dry pressure drop against the experimental data when using an adapted Periodic Representative Element.

For clearness, Fig. 4 also shows the results of the dry pressure drop of a Mellapak 500.Y column from Spiegel and Meier (1992), which is expected to be lower than the wet pressure drop. Particularly, Fig. 4 highlights that the discrepancy between dry and wet pressure drops amplifies for higher F-factor, and this is confirmed both by the Sulcol data and the VoF-LES model.

Fig. 4 presents one of the first validation of a full two-phase numerical model applied to an elementary packing cell against real data of the whole column.

The VoF-LES model is also checked against the partitioning of liquid and gas within the vertical conventional cell. Here, both the phases are expected to distribute evenly between the two connected channels due to the lack of preferential directions. Table 4 lists the distribution of the two phases in the $y$-channel and confirms an almost regular repartition.

The VoF model is always subject to mass-loss due to the surface sharpening algorithm and numerical diffusion of the VoF equation itself. Our typical run is a large-scale simulation, i.e. run over at least tens of thousands of timesteps (around 16,000) with a total of around $2 \cdot 10^5$ iterations. For the cases considered, the mass loss at the end of the simulation ranges between 3 and 6%, which is significantly small given the large size of the numerical run.

### 3.4. Wet-stage simulations with cross-flow

We consider the cross-flow geometry with the liquid phase, as depicted in Fig. 2. Periodic conditions with imposed pressure jump corresponding to the pressure drop $\Delta p$ previously found in the dry simulation, listed in Table 3, are used at the boundaries. Pressure and velocity distributions within each channel taken from the dry stage, as in Table 3, are imposed as initial condition for the gas phase. The initial film thickness follows Eq. (8). As explained at the end of Section 3.1, the actual F-factor in the wet stage is lower than the dry stage; Table 5 resumes therefore the F-factor computed *a posteriori* at liquid load $B = 130\ \mathrm{m^3/m^2/h}$, to be used from now onwards.

The wet simulations are inherently unsteady given several timescales present in the two-phase flow within the cell, i.e. the convective timescale dominated by the gas flow, viscous timescale at the liquid-gas interface and near the wall, the latter enabling the resolution of the interfacial and wall velocity profiles, respectively. As a suitable criterion to stop the simulation runs, we consider the

**Table 4**
Repartition of liquid and gas (divided by the total amount of each single phase) within the $y$-channel for the wet stage of conventional vertical counter-current flow. Data correspond to three points (forth to sixth red star) of Fig. 4.

| $F$ ($\sqrt{\mathrm{Pa}}$) | Liquid | Gas |
|---|---|---|
| 0.50 | 0.53 | 0.45 |
| 0.76 | 0.51 | 0.54 |
| 1.12 | 0.47 | 0.49 |

**Table 5**
Gas-phase Reynolds numbers with corresponding horizontal gas velocities and F-factor used in this study for the wet-stage simulations with cross-flow.

| | Test 1 | Test 2 | Test 3 |
|---|---|---|---|
| $Re_G$ | 270 | 680 | 1365 |
| $U_G$ (m/s) | 0.76 | 1.92 | 3.86 |
| $F$ ($\sqrt{\text{Pa}}$) | 0.82 | 2.06 | 4.13 |

time-evolution of the maximum liquid speed in the counter-current channel, i.e. $U_{Lmax}^{counter} = |\max[\mathbf{U}_L^{yCD}]|$, where $\mathbf{U}_L^{yCD}$ is taken along the plane perpendicular to the $y$ axis and crossing the segment $\overline{CD}$ shown in Fig. 2. Since the counter-current channel is subject to waves at a greater frequency due to counter/cross-shear from gas, it makes the liquid flow in this channel more complex. We consider that a quasi-steady state is achieved when the fluctuations in time of $U_{Lmax}^{counter}$ are small enough (under 5% as worst case) and the simulations are stopped. Fig. 5 shows that the stabilization of the flow is found rapidly, particularly at high gas Reynolds numbers, whereas at $Re_G = 270$ the plateau is less pronounced. For this $Re_G$, it seems that a longer calculation is required to get convergence of the liquid velocity. However, it must be noted that the horizontal axis in Fig. 5 represents passes, which is a time quantity indicating the time the maximum gas velocity takes to pass through the domain, i.e. $\delta/u_G$ with $\delta$ length of the grey-shaded channel defined in Fig. 2 and $u_G = U_G \cos\beta$ inlet gas velocity of the dry stage as in Table 2. Therefore, equal pass does not mean equal simulation time: the run at $Re_G = 270$ is longer than the others, given that $u_G$ is lower whereat the time for the gas to pass through the elementary cell is greater. Consequently, the choice of using passes as time unit for our simulations is a way to take into account the different convergence rate among all the performed runs. From Fig. 5, we have chosen to stop the simulations after 16 passes. This is equivalent to 16 cross-flow cells in a row in the results to follow.

## 4. Results and discussion

### 4.1. Analysis of the base configuration

In this section we perform an analysis of the base configuration, i.e. the three tests listed in Table 5 at liquid load $B = 130\ \text{m}^3/\text{m}^2/\text{h}$. We firstly compute the effective interfacial area ratio $E_A$, defined as

$$E_A = \frac{A_i}{S}, \tag{10}$$

where $A_i$ is the gas-liquid interfacial area predicted by the wet-stage simulation and $S$ the surface area of the wall of the packing, as introduced in Section 2. The surface area $S$ is constant and depends on the type of the structured packing. The gas-liquid interfacial area is computed as area of the iso-surface at volume fraction equal to 0.5, which corresponds to the interface. The effective interfacial area ratio $E_A$ gives an overview of the available gas-liquid exchange area. Fig. 6 shows that the time evolution of the interfacial area lies in the range $0.96 < E_A < 1.01$. More importantly, it is not affected by the gas load, which is in line with previous works, as Shulman et al. (1955) and Yoshida and Koyanagi (1962). This also matches the theoretical findings that the interfacial instabilities, i.e. the interfacial waves, are more influenced (dampened) by viscous dissipation in the liquid phase (Schmidt et al., 2016; Lavalle et al., 2017). An $E_A$ greater than the unit indicates a highly wavy interface which yields an interfacial area greater than the surface area of the packing. As expected, this is only possible at very high gas $Re_G$ where gas shear is considerable.

Fig. 6 also underlines the dynamic nature of the two-phase flow within the cell. This illustrates well the need to find a suitable criterion that is both representative of the physical gas-liquid interaction and is numerically stable enough.

The net pressure drop in the cross-flow cell is computed with the following definition:

$$G_{wet} = \frac{\Delta p_y + \Delta p_z}{2L}, \tag{11}$$

which is in line with dry simulation, i.e. Eq. (9). The net overall pressure drop (11) is then averaged in time in the range of 13–16 passes, with the aim to ignore the initial transient. Although Fig. 5 shows that the transient is much shorter, the maximum liquid speed $U_{Lmax}^{counter}$ depicted in Fig. 5 is averaged on the plane passing through $\overline{CD}$ and perpendicular to $y$. It can be expected that the flow has a longer transient locally. From now onwards we choose to average in the range of 13–16 passes as a safe criterion. Table 6 lists the pressure drop $G_{wet}$ at different gas Reynolds numbers, which in turn have been computed *a posteriori* as explained in Section 3.1. By comparing the wet pressure drop with the dry configuration (Table 3), we confirm that the dry and wet pressure drops computed by our VoF-LES model are almost identical because the dry pressure drop is imposed as boundary condition in the wet scenario. Finally, an analysis of the flow repartition within the two channels

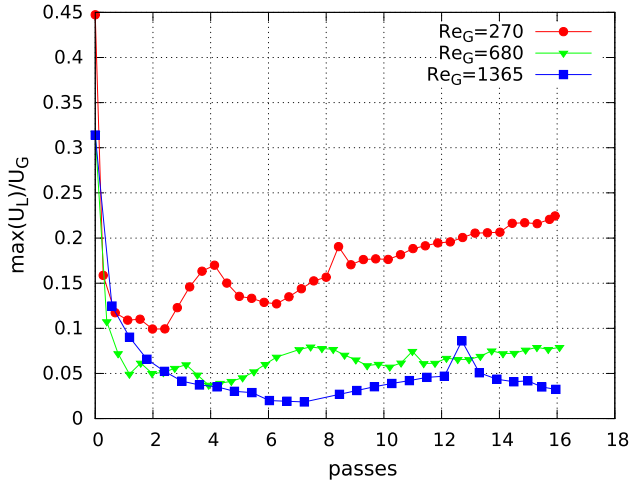


**Fig. 5.** Module of the maximum liquid velocity within the counter-flow channel averaged on the plane normal to the $y$ axis and passing by the points $C$ and $D$ of Fig. 2. The liquid velocity is scaled with the initial gas velocity, as in Table 2. One pass is defined as the time required by the gas to flow once through the channel.

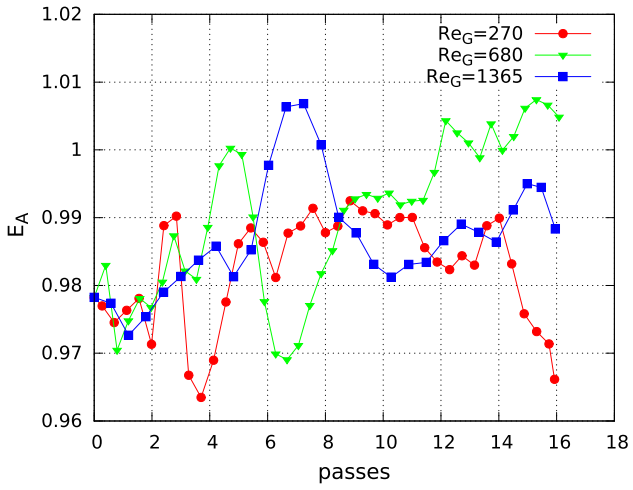


**Fig. 6.** Effective interfacial area ratio versus number of passes. One pass is defined as the time required by the gas to flow once through the channel.

**Table 6**
Wet simulation: time-averaged (in the range 13–16 passes) Reynolds number $Re_G$, pressure drop and flow repartition. Counter-current channel: $y$-direction; co-current channel: $z$-direction. By comparing this data with those in Table 3, one notes that $Re_G$ is smaller in the wet scenario at the same pressure drop.

| $Re_G$ | $G_{wet}$ (Pa/m) | $q_{Gy}/Q_G$ | $q_{Gz}/Q_G$ | $q_{Ly}/Q_L$ | $q_{Lz}/Q_L$ |
|---|---|---|---|---|---|
| 270 | −124.3 | 0.75 | 0.25 | 0.65 | 0.35 |
| 680 | −358.9 | 0.58 | 0.42 | 0.66 | 0.34 |
| 1365 | −786.5 | 0.62 | 0.38 | 0.65 | 0.35 |

of the elementary cell is provided in Table 6. Flow repartition $r$ is the ratio of the gas flow within the counter-current and co-current channels with respect to the total gas flow (the same also applies to the liquid phase):

$$r_{jy} = \frac{q_{jy}}{Q_j} \qquad r_{jz} = \frac{q_{jz}}{Q_j}, \tag{12}$$

where $j$ is the phase descriptor ($L$ liquid or $G$ gas), $q_{jy}$ and $q_{jz}$ are the mass flow rates in the considered channel (subscript $y$ for the counter-flow and $z$ for the co-flow channel), whereas $Q_j = q_{jy} + q_{jz}$ is the total amount for each phase. As before, the flow repartition is averaged in time in the range of 13–16 passes. We note that the liquid repartition is slightly affected by the gas load, whereas the gas repartition is influenced in much stronger way. Most of the gas flow is driven through the counter-current channel, in the upward direction. Indeed, in the region of the unit cell where both the channels meet and mix, the direction of the flow is neither fully vertical nor horizontal, resulting that an angle of $\beta = 45^\circ$ renders the counter-current channel to be preferential for the gas phase. At low liquid loads, one would expect that the liquid phase flows favourably in the co-current channel eluding the gas opposition of the counter-current channel. However, in this configuration the liquid load lies in the upper segment of the conventional absorption packings, i.e. $B = 130\ \mathrm{m^3/m^2/h}$, and the liquid Froude number $Fr_L = U_L^2/(gD) = 3.3$ shows that gravity is not dominant upon inertia in the liquid phase. Therefore, the liquid might be driven by the gas in the counter-current channel rather than by the gravity along the co-current channel. In addition, it is possible that some portions of liquid flow laterally in the channel due to the gas dynamics in the mixed channels. This effect increases at higher gas loads.

The time-averaged mass flow rate ratio for both the liquid and the gas in the range 13–16 passes for the counter-current channel are sketched in Fig. 7. From this diagram one recovers the regions where the gas and the liquid flow repartitions are similar. Particularly, with Fig. 7 we aim to perform a first step towards optimisation of the cross-flow cell. Our analysis is crucial towards the identification of the conditions at which a flow repartition as close as possible to 50% for both phases is achieved. We note that the liquid mass flow rate fluctuates around 64% and is slightly affected by the gas Reynolds number. The gas mass flow rate, instead, appears more uniform only in the range $Re_G = 650$—$1400$. We also note that starting from $Re_G = 971$ the liquid and gas repartitions are closer to each other, i.e. around 65% in the counter-current channel and almost 35% in the co-current channel. However, at large scale, this mass flow imbalance would potentially lead to the creation of a preferred pathway for the gas flow, causing a reduction of mass transfer performance. In addition, the poor percentage of liquid flow rate in the co-current channel could induce the formation of dry or partially dry areas, leading again to unfortunate conditions for mass transfer.

### 4.2. Influence of the tilting angle

We explore whether it is possible to achieve a better gas flow repartition by tilting the packing to use gravity to rebalance the liquid flow in both channels. Indeed, our goal is to achieve a flow repartition as close as possible to 50% for both phases. With reference to Fig. 2, the inclination of the cross-flow cell around the $x$ axis is varied along the tilting angle $\beta$ ($\beta > 45^\circ$ for clockwise tilting, and viceversa). With the aim to perform a sensitivity analysis of the inclination of the packing structure, we select the range $\beta = 30^\circ - 50^\circ$ and study the overall pressure drop, flow repartition and tendency to flooding.

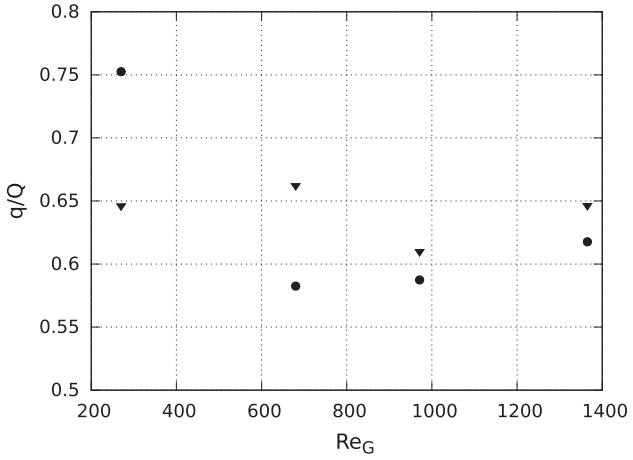


**Fig. 7.** Dimensionless mass flow rate in the counter-current channel averaged with passes 13–16: liquid phase (black triangles), gas phase (black circles). The dimensionless flow rate $q/Q$ is given by the ratio of the liquid (gas) flow rate in the counter-current channel divided by the total liquid (gas) flow rate within the cell.

Fig. 8 shows the contour lines of the overall wet pressure drop with respect to gas flow rate and tilting angle. At constant tilting angle, the pressure drop increases with the gas flow rate, which is to be expected; fixing the gas Reynolds number, the highest pressure drop is encountered at 45°; meanwhile, increasing or decreasing the tilting angle $\beta$ from this position appears to have the same benefit in terms of reducing the pressure drop. This is revealed by the slope of the contour lines in both the direction of tilting.

In order to estimate the direction of tilting leading to a repartition of gas and liquid as balanced as reasonably possible, we need to investigate the overall flow repartition with respect to $\beta$. Fig. 9

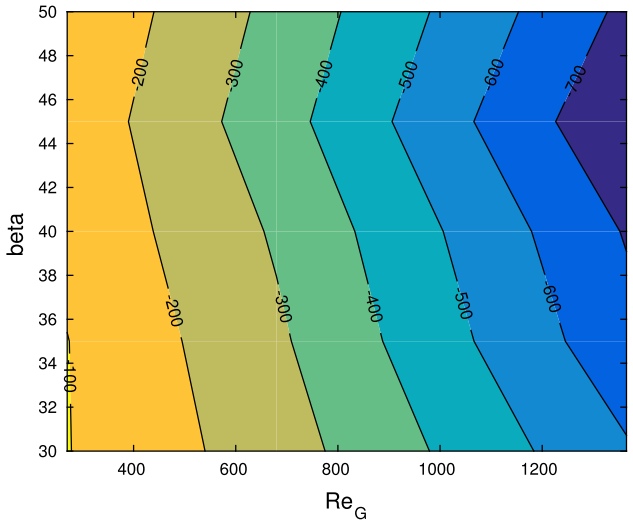


**Fig. 8.** Contour plot depicting time-averaged (in the range 13–16 passes) pressure gradient (in Pa $\mathrm{m^{-1}}$) as a function of tilting angle and gas Reynolds number.

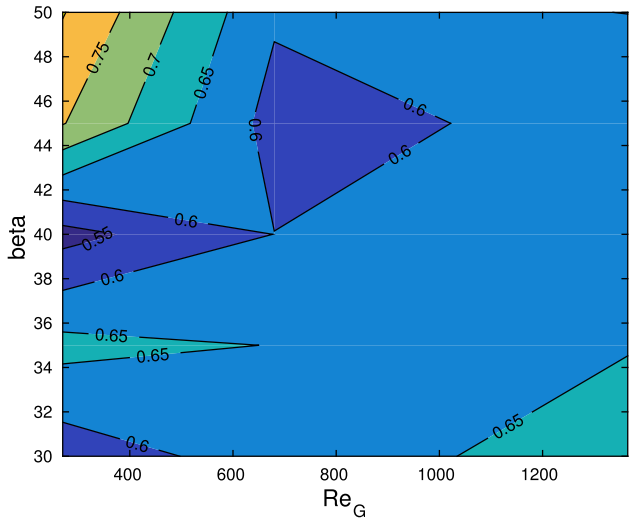


**Fig. 9.** Contour plot of the gas mass flow rate ratio in the counter-current channel at different tilting angles and gas Reynolds numbers, time-averaged in the range 13–16.

shows the averaged gas flow repartition in the counter-current channel in the range 13–16 passes for several tilting angles and gas flow rates. We note that, at small gas flow rates, the variation of the gas flow repartition with the tilting angle is more pronounced. This happens because, at high velocity, the gas is less inclined to be influenced by tilting. Indeed, an analysis of the Froude number (computed as $Fr_G = U_G^2/(gD)$, where the equivalent diameter $D$ is defined in Section 2) shows that $Fr_G = 290$ at $Re_G = 1365$ whereas $Fr_G = 11.3$ at $Re_G = 270$, which elucidates that the role of gravity is much smaller at high gas flow rates.

From Fig. 10 one notices that the liquid repartition weakly changes with the gas speed, although it is clear that the liquid phase is hindered in the counter-current channel as the gas load increases. This effect has been already discussed in the previous section for the case at 45°. On the contrary, the liquid flow repartition is strongly affected by the tilting angle, and the share of liquid in the counter-current channel tends to increase when the angle decreases, i.e. when the counter-current channel becomes more vertical. At this stage, this analysis has suggested that higher tilting angles and relatively high gas flow rates (compared to those of a typical vertical packing, to be shown in Section 5) are likely to provide better flow repartition and are to be preferred, although a 50–50% flow repartition would not be achievable without representing the contribution to flow repartition of perforations of the packing wall.

We also analyse the liquid velocity in the counter-current channel: this velocity is taken along the segment $\overline{CD}$ depicted in Fig. 2, which covers the counter-current channel from the edge to the centre of the cell. Along this line, we compute the average of the liquid velocity, which is time-averaged in range of 13–16 passes. Referring to Fig. 2, the sign of the velocity indicates its direction against the vertical coordinate $y$. Of particular interest is the gas velocity corresponding to an average liquid velocity of zero. At this point, two equal parts of liquid go down and up the counter-current channel, such that there is no net flow of liquid. It is referred further as the flooding point, although it is important to note that this does not necessarily correspond to a more practical definition related to a sharp increase in pressure drop as one observes in Fig. 4. It is also important to note that partial flow reversal in the liquid phase can be observed before the average velocity reaches zero, close to the gas–liquid interface. The corresponding contour lines are depicted in Fig. 11: when the gas flow rate increases the averaged velocity increases (decreases in amplitude). In this case the gas phase decelerates the liquid through counter-current shear. In addition, a tendency to flooding occurs when increasing the tilting angle, that is when the cross-flow cell is tilted clockwise. For example, the top right corner (i.e. at high gas flow rate and high tilting angle) is the worst configuration in terms of flooding among those investigated here. On the contrary, keeping the same gas flow rate while reducing the angle provides an amelioration in terms of flooding delay.

Finally, Fig. 12 sketches the velocity profile along the segment $\overline{CD}$ for both the liquid and the gas. The interface is located approximately at $x/d = 0.75$, where $x$ is the coordinate along the segment $\overline{CD}$ whereas $d$ its length (coinciding with the diagonal of the inlet triangle). The gas phase is located on the left and the liquid phase on the right. Also, $x/d = 0$ identifies the centre of the cell, i.e. the point $C$ depicted in Fig. 2. Here, the gas velocity eventually becomes negative due to the presence of recirculation eddies near the centre of the cell. From Fig. 12 we observe that the minimum

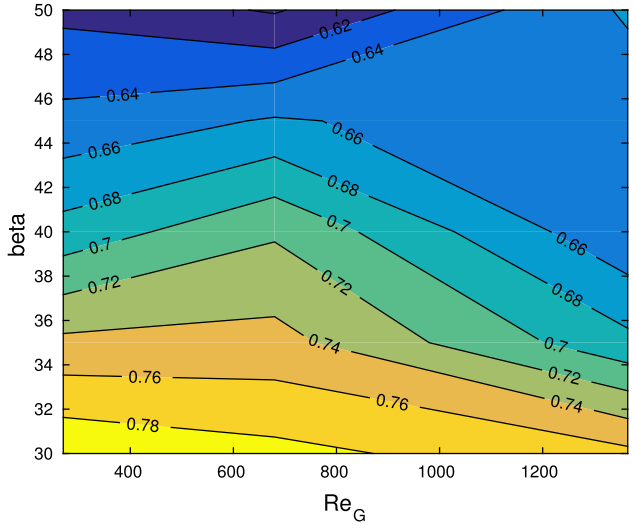


**Fig. 10.** Contour plot of the liquid mass flow rate ratio in the counter-current channel at different tilting angles and gas Reynolds numbers, time-averaged in the range 13–16.

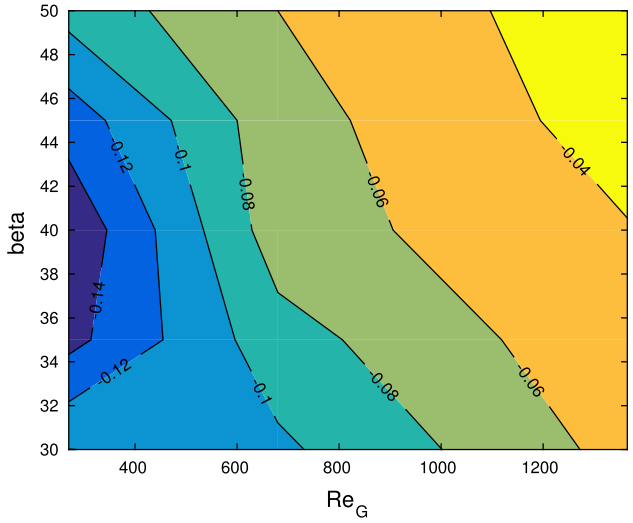


**Fig. 11.** Contour plot depicting line-averaged liquid velocity (scaled with $U_L = 0.4115$ m/s) in the counter-flow channel along the segment $\overline{CD}$, and time-averaged between passes 13–16. Lighter colors are indication of propensity to flooding.

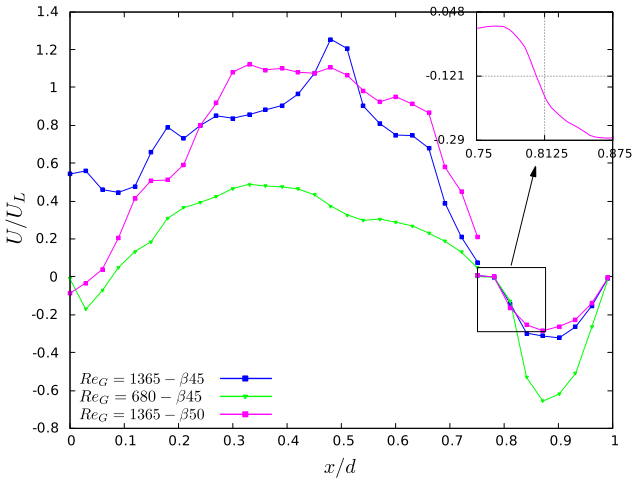


**Fig. 12.** Liquid and gas velocity profiles along the segment $\overline{CD}$ scaled with $U_L = 0.4115$ m/s. The gas velocity (at $x/d < 0.75$) has been also divided by 10 to simplify the visualisation. The length has been scaled with the diagonal of the inlet triangle $d = 0.0064$ m. Inset shows the incipient flow reversal of the configuration at $\beta = 50^\circ$ and $Re_G = 1365$, i.e. the top right corner of Fig. 11.

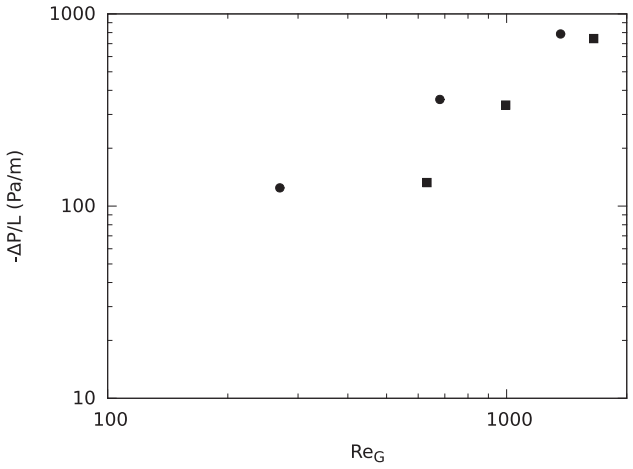


**Fig. 13.** Overall pressure-drop evolution for two liquid loads at different $Re_G$. Liquid load: $B = 1.3$ m$^3$/(m$^2$ h) black squares; $B = 130$ m$^3$/(m$^2$ h) black circles.

**Table 7**
Wet simulation at low liquid load $B = 1.3$ m$^3$/m$^2$/h: Reynolds number $Re_G$ recovered *a posteriori* and overall pressure drop $G_{wet}$.

| $Re_G$ | $G_{wet}$ (Pa/m) |
|---|---|
| 631 | −132.6 |
| 994 | −335.5 |
| 1652 | −744.4 |

value of the parabolic velocity profile of the liquid strongly decreases for smaller gas-phase Reynolds numbers. Varying the tilting angle at the same $Re_G$, the velocity profiles in the liquid phase are similar to each other, although the minimum slightly decreases when the tilting angle increases. This is also confirmed by the contour lines in Fig. 11. Particularly, from the zoomed velocity profile corresponding to the top right corner of Fig. 11, we observe the inception of the flow reversal, which occurs next to the interface. It gives a first hint for the characterization of the flooding onset. On the gas side, the velocity profile is fully turbulent. The effect of the tilting angle is weak on both the phases, whereas the influence of the gas Reynolds number is clear.

The analysis of the flooding onset has indeed revealed that small angles, i.e. a more vertical counter-flow channel, and low gas Reynolds numbers are to be preferred to avoid flow reversal. This is in conflict with the results previously discussed on flow repartition. Therefore, a compromise must be found to balance at the same time flow reversal, flow repartition and pressure drop.

Also, it must be recalled that holes on the wall of the packing are not represented in this transient two-phase VoF-LES model. They have a primary role to help the liquid drain, and it is expected that would improve the flow repartition in the cross-flow packing. This gives a reasonable argument for future studies aimed to model holes and textures on the packing wall, as well as for experimental studies.

### 4.3. Influence of the liquid load

The liquid load imposed in the previous test-cases is close to the upper limit of the applications of absorption and distillation, i.e. $B = 130$ m$^3$/m$^2$/h. In this section, we investigate the role of the liquid load on the overall pressure drop and the flooding, for the configuration with $\beta = 45^\circ$, by decreasing the liquid load of a factor 100, i.e. with $B = 1.3$ m$^3$/m$^2$/h, which remains still reasonable for chemical applications. As mentioned earlier, we stop the simulations before numerical break-up occurs in the liquid film. This is particularly important for low liquid loads where the film will be thin and has more propensity to numerically break-up. We are already running our simulations to account for maximum possible mesh density allowed by the commercial solver.

Fig. 13 sketches the overall pressure drop for these two liquid loads varying the gas Reynolds number. It would be desirable to provide results at the same gas Reynolds number. However, this is not possible since the wet gas Reynolds number is computed *a posteriori*, as mentioned earlier. The best we can do is to start with the same dry gas Reynolds number. This graph is supplemented by Table 6 for the high liquid load and by Table 7 for the small liquid load. We anticipate that the pressure drop should be smaller at low liquid loads, since the liquid that occupies the cell is less, as shown for example by Kolev and Razkazova-Velkova (2001). Likewise, in Fig. 13 we observe greater F-factor at small liquid load for the same pressure drop.

A sketch of the gas-liquid interface and of the gas-streamline distribution resulting from our numerical simulations is depicted in Fig. 14, where the effect of gas Reynolds number, tilting angle and liquid load is shown. We note that the interface is smooth and slightly corrugated in the sense of the gas flow for high liquid loads, whereas the interface is much more disturbed at low liquid loads. Secondly, the analysis of the streamlines in the gas phase highlights that the co-current channel and the counter-current channel behave very differently, in particular the flow in the counter-flow channel is more chaotic. This is expected to occur in a cross-flow cell but not in a "vertical" cell representative of a conventional counter-flow column configuration.

Comparing the four different cases, one also notices that the interface of the most inclined case in Fig. 14(e) strongly differs from the others: indeed the interface is more disturbed in the vicinity of the cell edge, as in presence of waves.

Interfacial waves are very important as those enhance the transfers between the two phases (Henstock and Hanratty, 1979; McCready and Hanratty, 1985). An analysis of the ratio $\epsilon = h/\lambda$ between the film thickness $h$ (measured as the maximum wave height observable in Fig. 14(e), i.e. $h_{max} = 1.2$ mm) and the wavelength $\lambda$ returns $\epsilon = 0.2$ in the co-current channel and $\epsilon = 0.1$ in the counter-current channel. The ratio $\epsilon$ emphasizes that those are likely to be long waves. It would be interesting to check

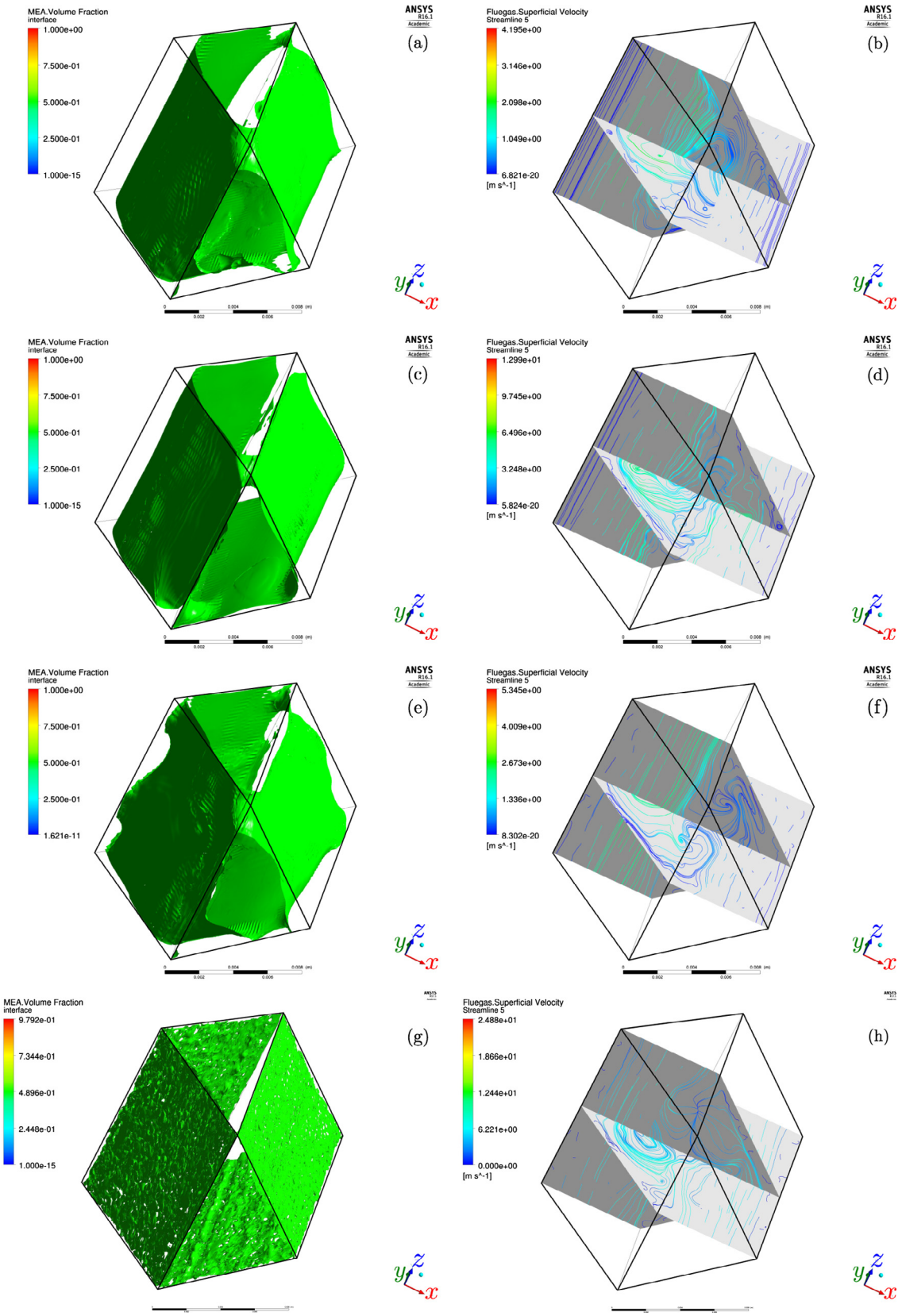


**Fig. 14.** Interface (left panel) and gas-streamline pattern (right panel) for different $Re_G$, angles and liquid loads: (a-b) $Re_G = 270, \beta = 45^\circ, B = 130\ m^3/m^2/h$; (c-d) $Re_G = 1365, \beta = 45^\circ, B = 130\ m^3/m^2/h$; (e-f) $Re_G = 270, \beta = 30^\circ, B = 130\ m^3/m^2/h$; (g-h) $Re_G = 1652, \beta = 45^\circ, B = 1.3\ m^3/m^2/h$. The interface is computed as the iso-surface of volume fraction at 0.5. Counter-current channel: $y$-direction; co-current channel: $z$-direction.

whether recirculation zones next to the interface are observable in both the phases, as those detected in vertical and inclined falling films sheared by a counter-current gas (Dietze and Ruyer-Quil, 2013; Trifonov, 2010; Lavalle et al., 2017). This could be improved by further refining the mesh, although the complexity of the computational domain would require too high computational resources for the actual run.

## 5. Comparing the cross-flow to conventional vertical packings

This section presents the comparison of the wet pressure drop of the cross-flow cell to different conventional vertical packings. Data of the pressure drop for those packings are taken from Bessou et al. (2010), at a liquid load of 7 $m^3/m^2/h$. In their work, Bessou et al. (2010) have compared the performances of the Sepcarb™ 4D structured packing to those of the random packing P-RING 5/8 and the structured Mellapak 250.Y and MellapakPlus™ 452.Y. In order to locate the cross-flow packing among the above-mentioned ones, we use the results of pressure drop obtained in the previous section at liquid load equal to 1.3 $m^3/m^2/h$. Although this is slightly different from the liquid load of Bessou et al. (2010), we can recover from Fig. 13 that the pressure drop obtained through the VoF-LES model will not be strongly affected by using 1.3 $m^3/m^2/h$ rather than 7 $m^3/m^2/h$. In addition, we show data of the pressure drop of the Sulzer MellapakCC™, taken from Menon and Duss (2011). The resulting comparison is depicted in Fig. 15. This is meant to be a qualitative comparison aiming to situate the cross-flow elementary cell of Mellapak 500.Y with the conventional structured and random packings. Indeed, both the size and the liquid load are different, particularly the data of the MellapakCC are obtained with a 3 m-high column with a diameter of 1 m filled with air and water; the liquid load is 25 $m^3/m^2/h$. As mentioned in Bessou et al. (2010), also the data from the packings Sepcarb 4D, P-RING 5/8, Sulzer M250.Y and M452.Y are obtained at different specific areas. From Fig. 15 one notes that our results lie in the range of the conventional structured and random packings. It is worth noting that the wet pressure drop of the cross-flow cell, whose geometry is close to Mellapak 500.Y, is expected to be higher than Mellapak 250.Y and Mellapak 452.Y, yet it is located between Mellapak 250.Y and MellapakCC. Particularly, it is much higher than the pressure drop for counter-flow packing optimised for carbon capture applications, e.g. the MellapakCC.

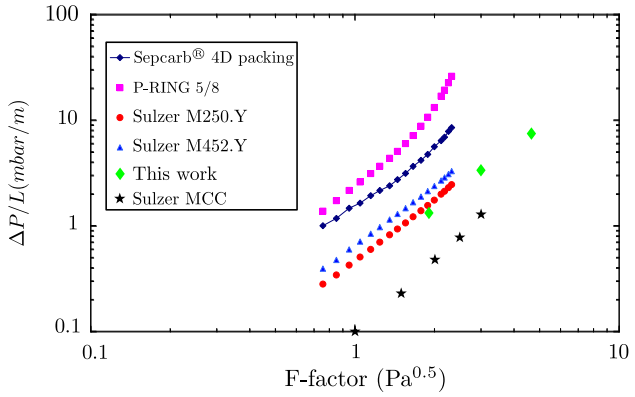


**Fig. 15.** Illustration of wet pressure drop between the cross-flow elementary cell (Mellapak 500.Y at a liquid load of 1.3$m^3/m^2/h$) and different structured packings: Sepcarb 4D, P-RING 5/8, Sulzer M250.Y and M452.Y at a liquid load of 7 $m^3/m^2/h$ from Bessou et al. (2010); MellapakCC at a liquid load of 25 $m^3/m^2/h$ from Menon and Duss (2011). Correspondence between F-factor, Reynolds number and external gas velocity is provided in Table 5.

## 6. Conclusions

This article provides novel and fundamental insights into a disruptive concept for contacting gas-liquid flows, where a compact, cross-flow, horizontal structure is streamlined to match the typical exhaust gas pathway of modern thermal power stations for carbon capture processes. It presents the performance of the three-dimensional cross-flow elementary cell of structured packings, in particular for the process intensification of post-combustion carbon capture. Dry and wet pressure drop, flow repartition and flooding onset are investigated through a full two-phase VoF-LES model. Due to the lack of data concerning the cross-flow packing, this model has been validated against previous numerical and experimental results in the vertical scenario.

Beginning with the base configuration at 45°, we have tested three different gas velocities, showing that the liquid and the gas flow repartitions within the two channels of the cell are not fairly balanced, ranging from 0.58 to 0.75 for high liquid loads. The cell is then tilted: the contour plot of the pressure drop shows that tilting the cell in both the direction (smaller and greater angles) reduces the pressure drop by 20% with respect to 45°. However, while the flow repartition improves at higher angles, the flooding is delayed at smaller tilting angle. This suggests that a compromise among pressure drop, flow repartition and flooding delay is necessary to detect the optimum configuration.

In addition, a sketch of the gas-liquid interface and the streamlines within the cell has revealed the presence of long waves at small tilting angles, which are known to enhance the transfer between the two phases.

The results presented in this work are characteristic of a single elementary three-dimensional cell. Therefore, further analysis with a scaled-up process model of absorption would complement this study and might indicate new pathway for optimisation. This article lays the foundation for further optimisation and refinement of the elementary cell. Packing holes or perforations are not represented in this study to limit the complexity of the numerical model. They are likely to help the drain of the liquid and improve the flow repartition within the cross-flow elementary cell. Likewise, the textures on the wall are not included either.

Finally, the geometry of the cell and, in particular, the angle between its channels offers scope for optimisation. The current configuration represents a packing with a Y shape. It is now clear that a packing with an X shape, where the two connected channels are not perpendicular, would change the two-phase flow dynamics completely, with the potential for further improvements.

Finally, the complex transient gas velocity field can be used as an input to our in-house reduced model SWANS, based on the coupling of a long-wave film model for the liquid phase to Navier-Stokes equations for the gas, and now tailored to counter-current flows (Lavalle et al., 2017). Such a reduced model will be vital for determining pressure drops and flow profiles quickly in a complex two-phase flow scenario. However, at the present stage, the SWANS model cannot be applied to complex geometries as those in this work, and to turbulent flows either. We leave therefore the enhanced SWANS model to future studies.

## Acknowledgements

The authors gratefully acknowledge the EPSRC SELECT project (EP/M001482/1) for funding this work. Dr. Mathieu Lucquiaud is funded by a Research Fellowship from the UK Royal Academy of Engineering.

## References


Abbott, M.B., Basco, D.R., 1989. Computational Fluid Dynamics – An Introduction for Engineers. Longman Scientific and Technical, Harlow.

Aferka, S., Viva, A., Brunazzi, E., Marchot, P., Crine, M., Toye, D., 2011. Tomographic measurement of liquid hold up and effective interfacial area distributions in a column packed with high performance structured packings. Chem. Eng. Sci. 66 (14), 3413–3422. 10th International Conference on Gas-Liquid and Gas-Liquid-Solid Reactor Engineering..

Amundsen, T.G., Øi, L.E., Eimer, D.A., 2009. Density and viscosity of monoethanolamine + water + carbon dioxide from (20 to 80) °C. J. Chem. Eng. Data 54, 3096–3100.

Ataki, A., Bart, H.-J., 2006. Experimental and CFD simulation study for the wetting of a structured packing element with liquids. Chem. Eng. Technol. 29 (3), 336–347.

Belcher, S.E., Hunt, J.C.R., 1998. Turbulent flow over hills and waves. Annu. Rev. Fluid Mech. 30 (1), 507–538.

Bessou, V., Rouzineau, D., Prévost, M., Abbé, F., Dumont, C., Maumus, J.-P., Meyer, M., 2010. Performance characteristics of a new structured packing. Chem. Eng. Sci. 65 (16), 4855–4865.

Boomkamp, P.A.M., Miesen, R.H.M., 1996. Classification of instabilities in parallel two-phase flow. Int. J. Multiphase Flow 22, 67–88.

Brackbill, J.U., Kothe, D.B., Zemach, C., 1992. A continuum method for modeling surface tension. J. Comput. Phys. 100, 335–354.

Bradtmöller, C., Janzen, A., Crine, M., Toye, D., Kenig, E., Scholl, S., 2015. Influence of viscosity on liquid flow inside structured packings. Indus. Eng. Chem. Res. 54 (10), 2803–2815.

Craik, A.D.D., 1966. Wind-generated waves in thin liquid films. J. Fluid Mech. 26 (02), 369–392.

Dankworth, D.C., Sundaresan, S., 1989. A macroscopic model for countercurrent gas-liquid flow in packed columns. AIChE J. 35 (8), 1282–1292.

Dietze, G.F., Ruyer-Quil, C., 2013. Wavy liquid films in interaction with a confined laminar gas flow. J. Fluid Mech. 722, 348–393.

Fernandes, J., Lisboa, P.F., Simões, P.C., Mota, J.P., Saatdjian, E., 2009. Application of CFD in the study of supercritical fluid extraction with structured packing: Wet pressure drop calculations. J. Supercrit. Fluids 50 (1), 61–68.

Fourati, M., Roig, V., Raynal, L., 2012. Experimental study of liquid spreading in structured packings. Chem. Eng. Sci. 80, 1–15.

Grünig, J., Kim, S.-J., Kraume, M., 2013. Liquid film flow on structured wires: Fluid dynamics and gas-side mass transfer. AIChE J. 59 (1), 295–302.

Haroun, Y., Legendre, D., Raynal, L., 2010. Direct numerical simulation of reactive absorption in gas-liquid flow on structured packing using interface capturing method. Chem. Eng. Sci. 65 (1), 351–356.

Haroun, Y., Raynal, L., 2016. Use of computational fluid dynamics for absorption packed column design. Oil Gas Sci. Technol. – Rev. IFP Energies nouvelles 71 (43).

Henstock, W.H., Hanratty, T.J., 1979. Gas absorption by a liquid layer flowing on the wall of a pipe. AIChE J. 25 (1), 122–131.

Hutton, B., Leung, L., Brooks, P., Nicklin, D., 1974. On flooding in packed columns. Chem. Eng. Sci. 29 (2), 493–500.

Iliuta, I., Larachi, F., Fourati, M., Raynal, L., Roig, V., 2014. Flooding limit in countercurrent gas-liquid structured packed beds-prediction from a linear stability analysis of an Eulerian two-fluid model. Chem. Eng. Sci. 120, 49–58.

Jayarathna, S.A., Weerasooriya, A., Dayarathna, S., Eimer, D.A., Melaaen, M.C., 2013. Densities and Surface Tensions of $CO_2$ Loaded Aqueous Monoethanolamine Solutions with $r = (0.2 to 0.7)$ at $T = (303.15–333.15)$ K. J. Chem. Eng. Data 58, 986–992.

Klingspor, J., Colley, D., Gray, S., Brown, G., Lowell, P., 2002. Horizontal scrubber system. US Patent App. 10/002,881.

Kolev, N., Razkazova-Velkova, E., 2001. A new column packing for operation at extremely low liquid loads. Chem. Eng. Process.: Process Intensif. 40 (5), 471–476.

Labourasse, E., Lacanette, D., Toutant, A., Lubin, P., Vincent, S., Lebaigue, O., Caltagirone, J.-P., Sagaut, P., 2007. Towards large eddy simulation of isothermal two-phase flows: governing equations and a priori tests. Int. J. Multiphase Flow 33 (1), 1–39.

Lavalle, G., Vila, J.P., Lucquiaud, M., Valluri, P., 2017. Ultraefficient reduced model for countercurrent two-layer flows. Phys. Rev. Fluids 2.

Liovic, P., Lakehal, D., 2007a. Interface-turbulence interactions in large-scale bubbling processes. Int. J. Heat Fluid Flow 28 (1), 127–144.

Liovic, P., Lakehal, D., 2007b. Multi-physics treatment in the vicinity of arbitrarily deformable gas-liquid interfaces. J. Comput. Phys. 222 (2), 504–535.

McCready, M.J., Hanratty, T.J., 1985. Effect of air shear on gas absorption by a liquid film. AIChE J. 31, 2066.

Menon, A., Duss, M., 2011. The new Sulzer MellapakCC and AYPlusDC structured packings for post-combustion capture. In: IEAGHG 1st Post Combustion Capture Conference, 17–19 May, Abu Dhabi, UAE.

Nicolaiewsky, E.M., Tavares, F.W., Rajagopal, K., Fair, J.R., 1999. Liquid film flow and area generation in structured packed columns. Powder Technol. 104 (1), 84–94.

Nusselt, W., 1916. Die Oberflachenkondensation des Wasserdampfes. VDI-Zeitschrift 60, 541–546, english translation by D. Fullarton in Chem. Eng. Fund., 1 (2), pp. 6–19, 1982.

Olujić, Z., Seibert, A., Kaibel, B., Jansen, H., Rietfort, T., Zich, E., 2003. Performance characteristics of a new high capacity structured packing. Chem. Eng. Process.: Process Intensif. 42 (1), 55–60.

Petre, C., Larachi, F., Iliuta, I., Grandjean, B., 2003. Pressure drop through structured packings: breakdown into the contributing mechanisms by cfd modeling. Chem. Eng. Sci. 58, 163–177.

Raynal, L., Boyer, C., Ballaguet, J.-P., 2004. Liquid holdup and pressure drop determination in structured packing with cfd simulations. Canad. J. Chem. Eng. 82, 871–879.

Raynal, L., Royon-Lebeaud, A., 2007. A multi-scale approach for CFD calculations of gas-liquid flow within large size column equipped with structured packing. Chem. Eng. Sci. 62 (24), 7196–7204.

Said, W., Nemer, M., Clodic, D., 2011. Modeling of dry pressure drop for fully developed gas flow in structured packing using cfd simulations. Chem. Eng. Sci. 66, 2107–2117.

Scardovelli, R., Zaleski, S., 1999. Direct numerical simulation of free-surface and interfacial flow. Annu. Rev. Fluid Mech. 31, 567–603.

Schmidt, P., Ó Náraigh, L., Lucquiaud, M., Valluri, P., 2016. Linear and nonlinear instability in vertical counter-current laminar gas-liquid flows. Phys. Fluids, 28.

Sherwood, T.K., Shipley, G.H., Holloway, F.A.L., 1938. Flooding velocities in packed columns. Indus. Eng. Chem. 30 (7), 765–769.

Shulman, H.L., Ullrich, C.F., Proulx, A.Z., Zimmerman, J.O., 1955. Performance of packed columns. ii. wetted and effective-interfacial areas, gas - and liquid-phase mass transfer rates. AIChE J. 1 (2), 253–258.

Smagorinsky, J., 1963. General circulation experiments with the primitive equations. Month. Weather Rev. 91, 99–164.

Spiegel, L., Meier, W., 1992. A generalized pressure drop model for structured packings. In: IChemE Symposium Series. No. 128.

Tilley, B.S., Davis, S.H., Bankoff, S.G., 1994. Linear stability theory of two-layer fluid flow in an inclined channel. Phys. Fluids 6 (12), 3906–3922.

Trifonov, Y.Y., 2010. Flooding in two-phase counter-current flows: Numerical investigation of the gas-liquid wavy interface using the Navier-Stokes equations. Int. J. Multiph. Flow, 36.

Tseluiko, D., Kalliadasis, S., 2011. Nonlinear waves in counter-current gas-liquid film flow. J. Fluid Mech. 673, 19–59.

Valluri, P., Matar, O.K., Hewitt, G.F., Mendes, M., 2005. Thin film flow over structured packings at moderate reynolds numbers. Chem. Eng. Sci. 60 (7), 1965–1975.

Valluri, P., Ó Náraigh, L., Ding, H., Spelt, P.D.M., 2010. Linear and nonlinear spatio-temporal instability in laminar two-layer flows. J. Fluid Mech. 656 (2010), 458–480.

Vellingiri, R., Tseluiko, D., Kalliadasis, S., 2015. Absolute and convective instabilities in counter-current gas-liquid film flows. J. Fluid Mech. 763, 166–201.

Xu, Y.Y., Paschke, S., Repke, J.-U., Yuan, J.Q., Wozny, G., 2008. Portraying the countercurrent flow on packings by three-dimensional computational fluid dynamics simulations. Chem. Eng. Technol. 31 (10), 1445–1452.

Yih, C.-S., 1967. Instability due to viscosity stratification. J. Fluid Mech. 27, 337–352.

Yoshida, F., Koyanagi, T., 1962. Mass transfer and effective interfacial areas in packed columns. AIChE J. 8 (3), 309–316.